Kavli Summer Program in Astrophysics 2021
Fluid Dynamics of the Sun and Stars
Virtual school (MPS Goettingen)

Direct Numerical Simulations of vertical and horizontal shear instabilities

June 7th - July 16th, 2021

Saniya Khan
University of Birmingham

Pascale Garaud
UC Santa Cruz

1 Introduction

Today, our understanding of the general evolution of low-mass stars may be considered as fairly advanced. Stellar evolution codes are able to model the complete evolution of such stars, from the pre-main sequence phase to the white dwarf stage, and explain general properties such as their effective temperature and luminosity. But if we move from the broad picture to more detailed aspects of the evolution, strong weaknesses in the modelling of fluid dynamics appear at various evolutionary stages, affecting the treatment of convective processes but also of turbulent mixing in convectively-stable regions.

With the advent of recent and precise observational constraints from asteroseismology and spectroscopy, it has been noted that observations of surface abundances of some chemical elements and of subsurface flows cannot be explained by standard models only. Following this, several studies have thus suggested that the inclusion of turbulent mixing in the stably-stratified regions of stars could be a way to solve these discrepancies.

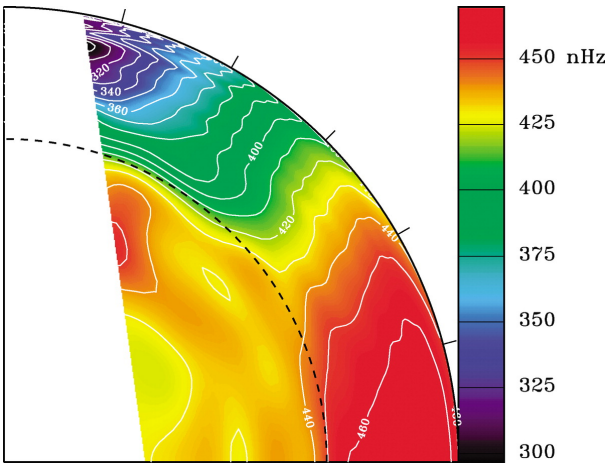

Figure 1: *Picture of the internal rotation of the Sun, as obtained from helioseismology. Figure taken from Schou et al. (1998).*

One very well-studied case where turbulent mixing is known to be important is that of the solar tachocline. As illustrated by helioseismic observations, the envelope of the Sun displays a differential rotation profile with equatorial regions rotating more rapidly ($\Omega_{\rm eq} \sim 450\,$nHz) with respect to polar regions ($\Omega_{\rm pole} \sim 350\,$nHz; Fig. 1). Just below the base of the convective envelope lies the solar tachocline, which is known to be a very strong vertical and horizontal shear layer. Another evidence for turbulent mixing related to the tachocline region comes from helioseismic observations of the solar sound speed profile. Comparisons of the observed and predicted sound speed show a significant discrepancy just below the base of the convective zone ($r_{\rm BCZ} \sim 0.71\,{\rm R}_\odot$), which can be straightforwardly related to the location of the tachocline (e.g. Christensen-Dalsgaard et al., 2018, see Fig. 2). This discrepancy is again telling us that some mixing process is missing in our current standard model of the Sun.

Former studies, such as Spiegel & Zahn (1992), have shown that in a standard picture of the Sun, in the absence of turbulent mixing, one would see a similar differential rotation profile from the convective zone to at least halfway to the solar centre. That would still be the case if one were to include isotropic turbulence which acts equally in the vertical and horizontal directions. By contrast, if one considers anisotropic turbulence whereby the horizontal component is much stronger than the vertical one, the tachocline region can actually be reproduced and limit the

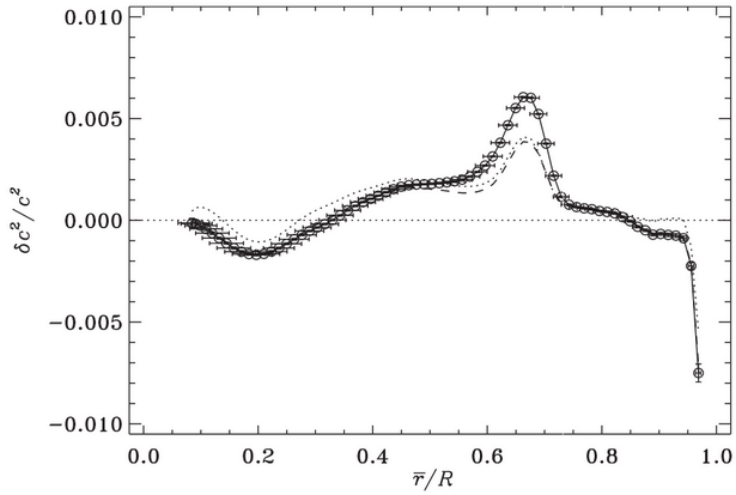

Figure 2: *Relative difference between the observed and predicted sound speed as a function of the normalised solar radius. The base of the convective zone is located at* $r_{\mathrm{BCZ}} \sim 0.71\,\mathrm{R}_\odot$. *Figure taken from Christensen-Dalsgaard et al. (2018).*

spread of differential rotation in the inner parts of the Sun, as shown on Fig. 3. Hence, the missing mixing process, suggested by helioseismic observations, could be related to shear-induced, strongly anisotropic turbulence.

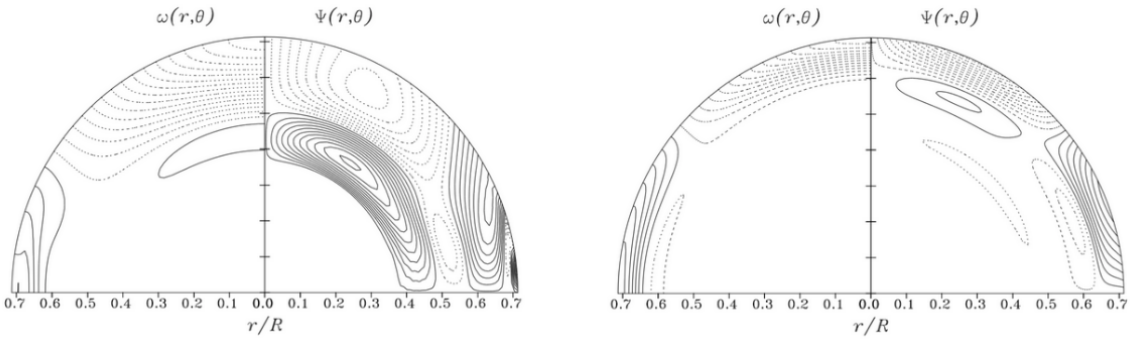

Figure 3: *Illustration of the spreading of differential rotation below the base of the convectize zone, at the current age of the Sun, with isotropic (left) or anisotropic turbulence (right). Figure taken from Elliott (1997).*

Motivated by these findings, several studies have been dedicated to the analysis of Direct Numerical Simulations (DNSs) of shear instabilities to determine how much mixing they cause. Studies from Prat & Lignières (2013, 2014), and also Garaud et al. (2017), have suggested that turbulence as induced by vertical shear instabilities is not very efficient. On the contrary, horizontal shear instabilities are potentially more relevant to stellar evolution. Recents works by Cope et al. (2020) and Garaud (2020) have tested a model for vertical mixing by horizontal shear instabilities, that was initially proposed by Zahn (1992). Fig. 4 shows simulation snapshots from Cope et al. (2020) in the stratified turbulent regime; the large-scale horizontal meanders decouple in the vertical direction, and lead to small-scale vertical mixing. Garaud (2020) identified different regimes of turbulence via horizontal shear instabilities (see Fig. 5). In

particular, they found the solar tachocline to be located in the non-thermally diffusive regime, at rather high Péclet numbers — which will thus be the focus of the current study. As part of her study, Garaud (2020) derived scaling laws for the RMS vertical velocity, vertical eddy scale, and RMS temperature as a function of the buoyancy parameter B (Fig. 6). Simulations deviating from these laws either fall in the weakly-stratified regime, at very low values of B, or in the viscously-dominated regime.

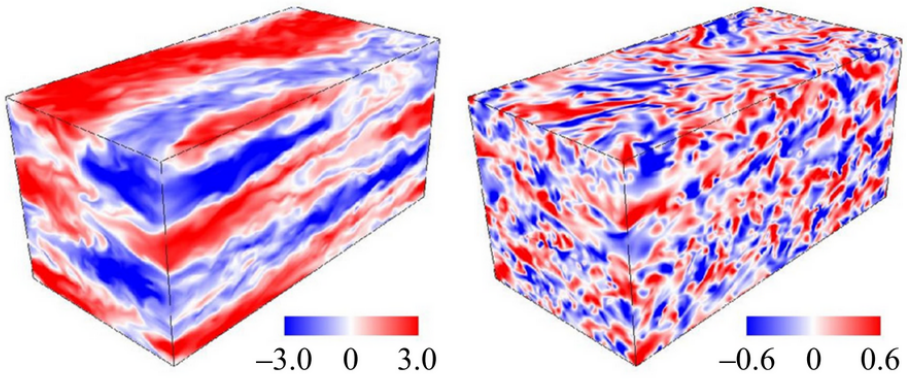

Figure 4: *Snapshots of the streamwise velocity (left) and vertical velocity (right) during the statistically-stationary states of DNSs of horizontal shear in the stratified turbulent regime. Figure taken from Cope et al. (2020).*

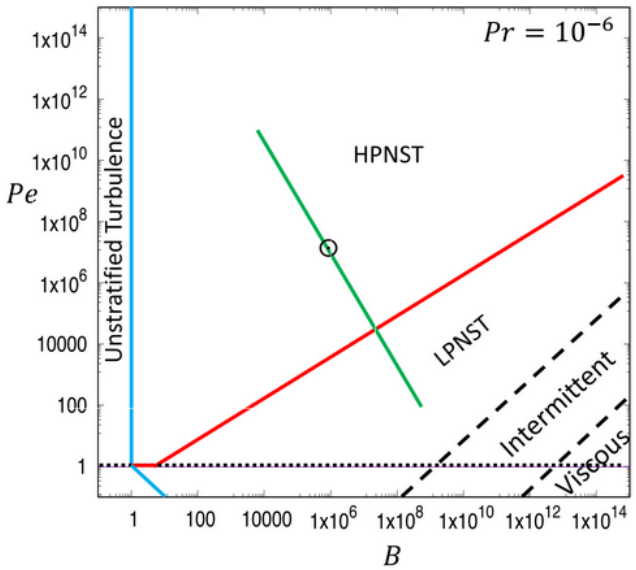

Figure 5: *Péclet number (quantifying the efficiency of thermal diffusion) as a function of the buoyancy parameter (as a measure of the stratification), illustrating the different regimes of turbulence via horizontal shear instabilities at a given Prandtl number: $Pr = 10^{-6}$. The latter measures the ratio between viscous diffusion and thermal diffusion, and a low value is appropriate for stellar interiors. HPNST (LPNST) corresponds to the high (low) Péclet number stratified turbulence regime. Figure taken from Garaud (2020).*

From these studies, it seems clear that vertical shear instabilities alone are not important

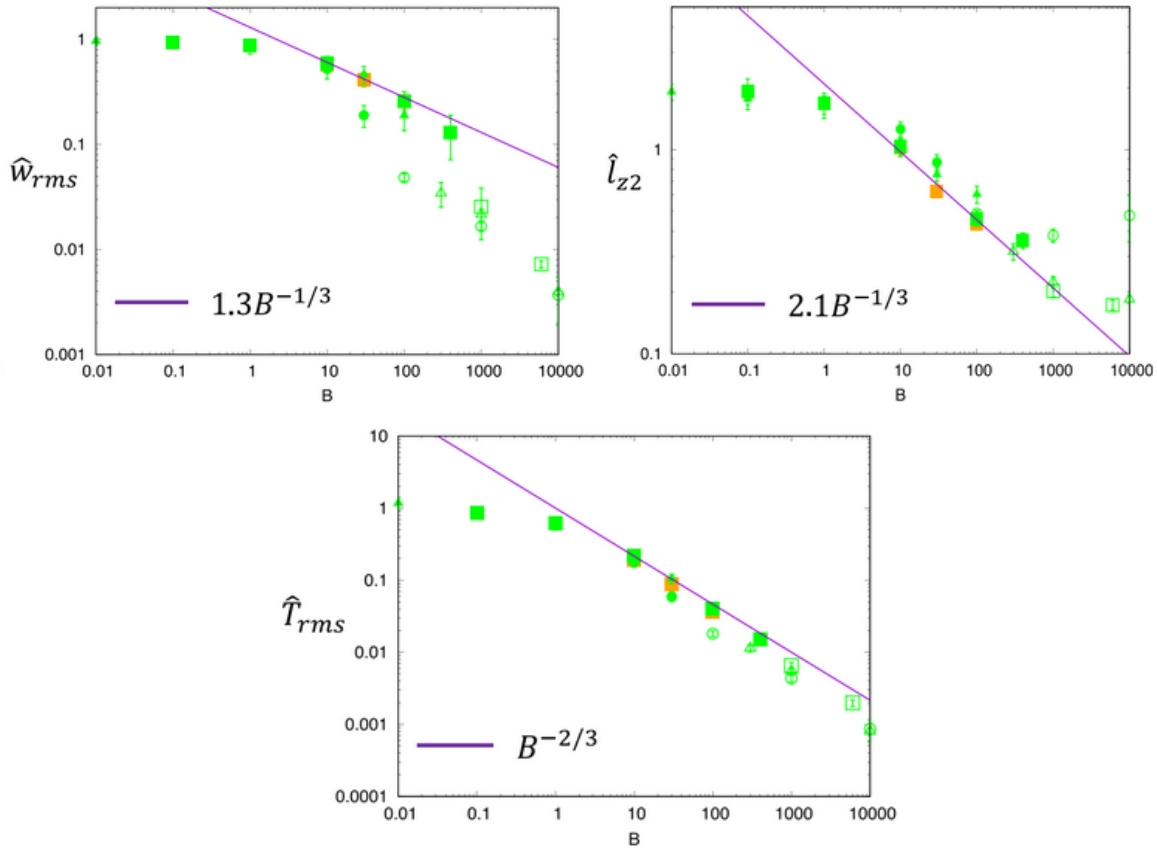

Figure 6: *RMS vertical velocity (top left), vertical eddy scale (top right), and RMS temperature (bottom), as a function of the buoyancy parameter. Triangles and squares correspond to* $Re = 300$ *and* $Re = 600$ *simulations, respectively. The purple lines represent fits to the data. Figure taken from Garaud (2020).*

enough. Meanwhile, horizontal shear instabilities can constitute a significant source of turbulent mixing in stars, although they do not provide the anisotropy needed in order to reproduce the present-day tachocline (Garaud, 2020). Additional effects still need to be taken into account, including magnetic fields and rotation. In particular, what happens when vertical and horizontal shear are combined together remains to be determined.

Hence, in this study, we analyse Direct Numerical Simulations of this combined vertical and horizontal shear in the high Péclet regime. Sec. 2 briefly describes the setup used for our numerical simulations of vertical and horizontal shear instabilities. Sec. 3 presents some of our simulations, as well as the method employed to extract the average parameters. Sec. 4 analyses the results and gives a comparison with the purely horizontal shear case from Garaud (2020). Finally, Sec. 5 concludes our investigation by discussing possible implications for the Sun and other stars.

2 Model setup

The non-dimensional governing equations for our study are the following, the momentum equation (Eq. 1), the incompressibility condition for Boussinesq fluids (Eq. 2), and the temperature equation (Eq. 3):

$$\frac{\partial \hat{\mathbf{u}}}{\partial t} + \hat{\mathbf{u}} \cdot \nabla \hat{\mathbf{u}} = -\nabla \hat{p} + B\hat{T}\mathbf{e}_z + Re^{-1}\nabla^2 \hat{\mathbf{u}} + \sin(y + z\tan\theta)\mathbf{e}_x \,, \tag{1}$$

$$\nabla \cdot \hat{\mathbf{u}} = 0 \,, \tag{2}$$

$$\frac{\partial \hat{T}}{\partial t} + \hat{\mathbf{u}} \cdot \nabla \hat{T} + \hat{w} = Pe^{-1}\nabla^2 \hat{T} \,. \tag{3}$$

These equations have been non-dimensionalised using the anticipated amplitude of the flow U_F (Eq. 4), obtained by requiring a balance between the inertial terms and the forcing in the x direction:

$$U_\mathrm{F} = \left(\frac{F_0}{\rho_m k_s}\right)^{1/2} , \tag{4}$$

where F_0 is the amplitude of the sinusoidal body force driving the shear ($\mathbf{F} = F_0 \sin(y + z\tan\theta)$), ρ_m is the mean density of the region, and $k_s = 2\pi/L_y$ is the wavenumber associated with the domain width L_y.

Several parameters are introduced in these equations; the Reynolds number Re, the ratio of the viscous diffusion timescale to the turbulent advection timescale; the Péclet number Pe, the ratio of the thermal diffusion timescale to the turbulent advection timescale; and the buoyancy parameter B, the square of the ratio of the Brunt-Väisälä frequency N to the unit shearing rate (equivalent to the Richardson number but for horizontal shear):

$$Re = \frac{U_\mathrm{F}}{k_s \nu} \,, \quad Pe = \frac{U_\mathrm{F}}{k_s \kappa_T} \quad \text{and} \quad B = \frac{N^2}{k_s^2 U_\mathrm{F}^2} \,. \tag{5}$$

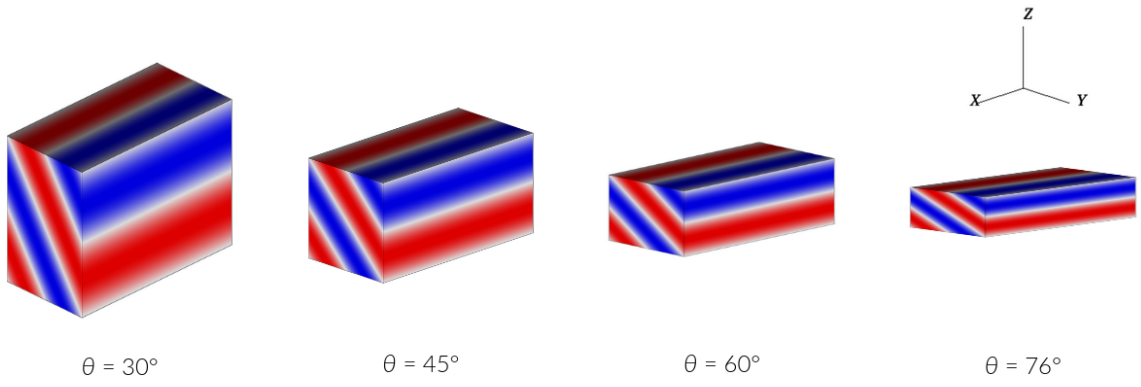

Figure 7: *Schematics of the basic state set-up showing the laminar body-forced velocity profile, in the different configurations:* $\theta = 30, 45, 60, 76°$.

The last term on the right hand side of the momentum equation (Eq. 1) is a forcing term accounting for combined vertical and horizontal shear instabilities, through a sinusoidal function and with a dependence on the inclination angle θ. Because of this, four different geometries are considered, for $\theta = 30, 45, 60, 76°$, as shown on Fig. 7. This setup is chosen so that the background flow is triply periodic, which is necessary for our code. It is sinusoidal in both directions, and by adjusting the height of the box L_z we can create larger shear (smaller L_z)

or weaker shear (larger L_z). The angle θ is defined such that $\tan\theta = L_y/L_z$. The maximum shearing rate in the horizontal direction is simply 1 in these units, and the maximum shearing rate in the vertical direction is thus $1/\tan\theta$. These could be considered as angles of inclination of the box in the Sun. In addition to the four inclination angles considered, we have run simulations for three different Reynolds numbers: $Re = 100, 330, 600$, associated with three Péclet numbers: $Pe = 10, 33, 60$, and for four different buoyancy parameters: $B = 1, 10, 100, 1000$. In what follows, however, we will not discuss the $Re = 100$ simulations, as most of these fall in the viscously-dominated regime. With all of this, we have a set of simulations that is comparable to that of Garaud (2020), but with different vertical shearing rates in addition to the horizontal shear.

3 Data analysis

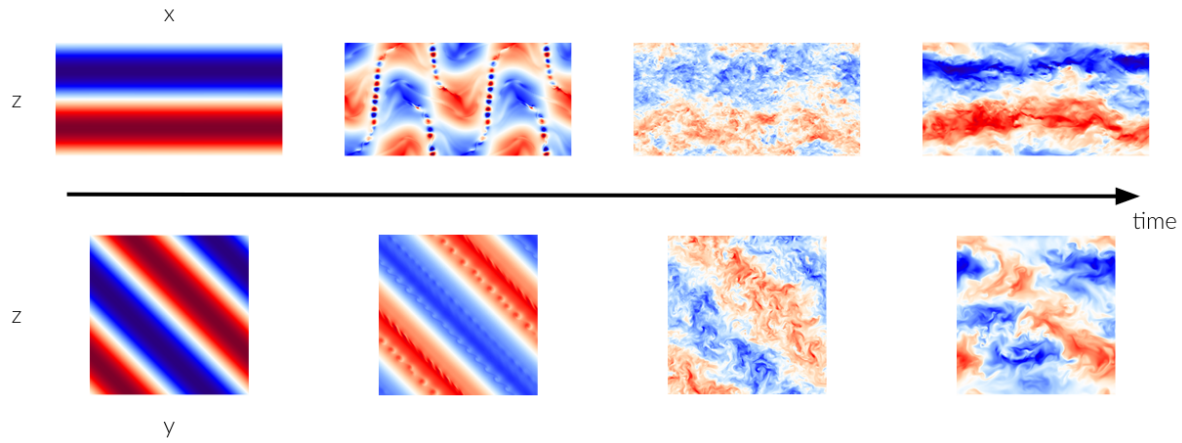

Figure 8: *Snapshots for the simulation with the following parameters:* $Re = 600, Pe = 60, B = 10, \theta = 45°$*, as it evolves with time (from left to right). The colour represents the streamwise velocity. The top and bottom rows show side views of the box along the streamwise and cross-streamwise directions, respectively. See text for details.*

Fig. 8 shows snapshots for the $Re = 600, Pe = 60, B = 10, \theta = 45°$ simulation. The top row shows side views of the box along the streamwise direction ($x - z$ plane) and the bottom row along the cross-streamwise direction ($y - z$ plane), at different times of the simulation. The first snapshots show the initial conditions defined by the forcing term in Eq. 1. The second snapshots illustrate the development of the primary and secondary instabilities. The third snapshots show an already pretty turbulent flow. And, lastly, the simulation is run until we reach a statistically-stationary state, corresponding to the final snapshots.

In order to illustrate this, Fig. 9 (left panel) shows the RMS vertical velocity as a function of time, for the same simulation. We clearly see the initial exponential growth of the instability followed by its nonlinear saturation into a statistically-stationary state. Once that state is reached, we then choose a time interval, indicated by the dashed lines, and compute the time-average and the RMS variability around the mean for this quantity, as well as other parameters including the RMS total velocity, the temperature dissipation rate, etc. This is done for each individual simulation.

Another quantity of interest is the vertical length scale of the eddies. To calculate this, following Garaud et al. (2017), we compute the autocorrelation function in the z-direction of

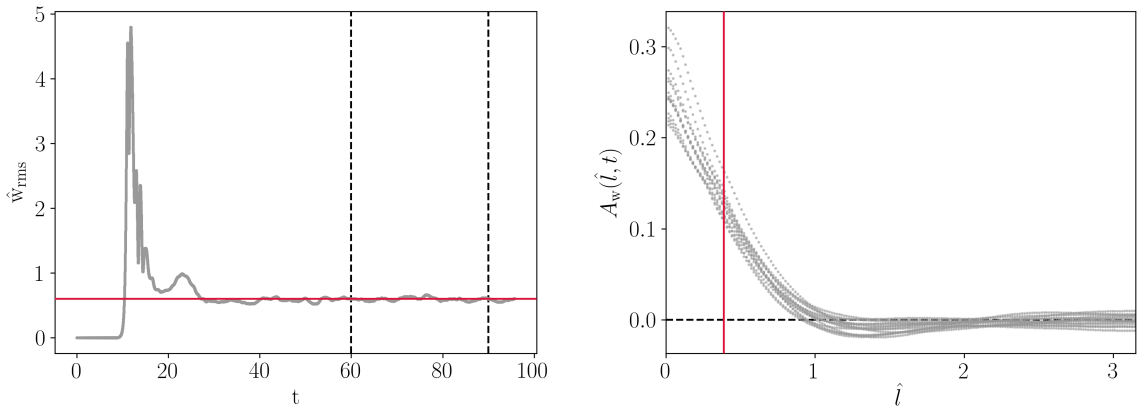

Figure 9: *Left: RMS vertical velocity as a function of time. The red line shows the mean value computed in the time interval chosen (vertical dashed lines). Right: Autocorrelation functions in the z-direction at different timesteps. The red line indicates the resulting estimate for the vertical eddy scale. These profiles are extracted from the simulation shown in Fig. 8.*

the vertical velocity, which is an integral over the whole domain and has the following expression:

$$A_w(\hat{l}, t) = \langle \hat{w}(x, y, z, t)\hat{w}(x, y, z + \hat{l}, t)\rangle \,. \tag{6}$$

An example of these is shown on Fig. 9 (right panel). Each line corresponds to an autocorrelation function at a different timestep. The vertical eddy scale at a particular time t is taken as the width at half maximum ($A_w(\hat{l}'_z, t) = 0.5A_w(0, t)$). We then estimate the average of these values in the statistically-stationary state and report this as the vertical eddy scale, indicated by the vertical red line.

4 Results

Fig. 10 shows the results obtained for the RMS vertical velocity, the vertical eddy scale, and the RMS temperature, as a function of the buoyancy parameter. As B increases, we see that all three parameters decrease. We do not see much scatter in the case of the RMS vertical velocity and RMS temperature, between the different inclination angles. However, for $B = 1$, we note a significant spread in the vertical eddy scale estimates, which is expected from the more weakly-stratified case. But, already from $B = 10$, most inclination angles tend towards the purely horizontal shear case, except for $\theta = 76°$.

To further illustrate this, Fig. 11 shows two snapshots with a side view of the box in the cross-streamwise direction ($x - z$), for $Re = 600, Pe = 60, \theta = 45°$, and $B = 1$ or $B = 100$. For $B = 1$, the background shear is quite apparent and controls the dynamics, which explains why the vertical eddy scale estimates vary with the inclination angle. On the contrary, at higher stratification parameters, such as $B = 100$, the background shear is not apparent anymore. Instead, there are horizontal meanders at different phases which determine the vertical eddy scale and, consequently, it is the emergent vertical shear due to these meanders, rather than the imposed vertical shear, that controls the vertical mixing. In other words, for strong stratification, the vertical shear does not affect the results.

On Fig. 12 we show the vertical eddy scale as a function of the stratification, but with additional lines giving an estimate of the background shear length scale, namely $\pi/4 \tan\theta$. Eddy

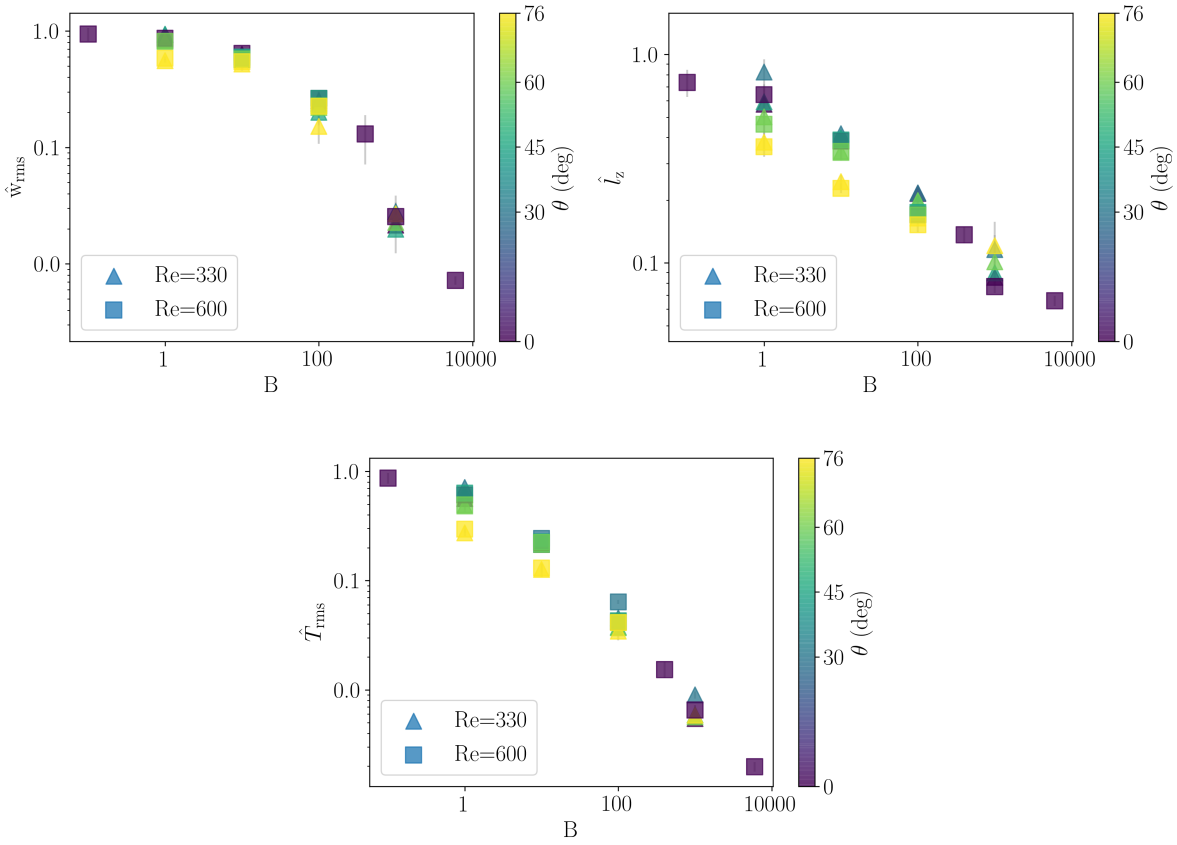

Figure 10: *RMS vertical velocity (top left), vertical eddy scale (top right), and RMS temperature (bottom), as a function of the buoyancy parameter. Triangles and squares correspond to* $Re = 330$ *and* $Re = 600$ *simulations, respectively. The colour scale indicates the inclination angle, with purple points corresponding to the pure horizontal shear case, for which additional values for intermediate stratifications have been derived.*

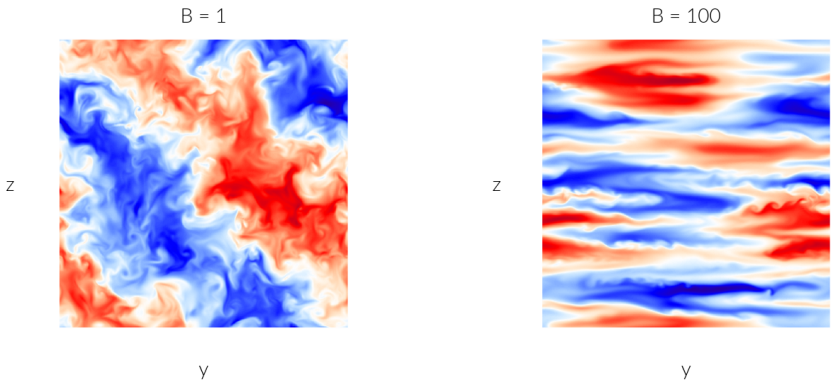

Figure 11: *Snapshots of the side view of the box in the cross-streamwise direction* $(x - z)$*, for the* $Re = 600, Pe = 60, \theta = 45°$*, and* $B = 1$ *(left) or* $B = 100$ *(right) simulations, during their statistically-stationary state. The colour represents the streamwise velocity.*

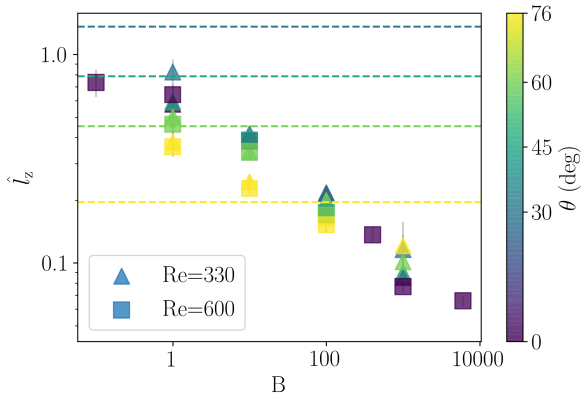

Figure 12: *Vertical eddy scale as a function of the buoyancy parameter. The horizontal lines give an estimate of the background shear length scale at each inclination angle. The symbols and colours are the same as in Fig. 10.*

scales larger than the corresponding background shear length scale, at the same inclination angle, feel the background shear and deviate from the pure horizontal shear case — as is the case for $B = 1, \theta = 76°$. On the other hand, eddy scales smaller than the background shear length scale do not feel it, and tend towards the case where $\theta = 0°$.

In summary:

– if the eddy scale is larger than the background shear scale, vertical shear will have an influence and should be considered;

– but if the eddy scale is lower than the background shear scale, vertical shear is negligible, which means that scaling laws derived by Garaud (2020) in the context of horizontal shear continue to apply.

5 Conclusions

From estimates of the internal rotation of the Sun ($\Omega_{\rm eq} \sim 450 \times 10^{-9}\,{\rm s}^{-1}$ and $\Omega_{\rm pole} \sim 350 \times 10^{-9}\,{\rm s}^{-1}$) and of the Brunt-Väisälä frequency in the tachocline region ($N \sim 10^{-3}\,{\rm s}^{-1}$), one can estimate the buoyancy parameter to be $B \sim N^2/\Delta\Omega^2 \sim 10^8$. The vertical length scale can then be approximated as $l_z \sim B^{-1/3} L$ (Garaud, 2020), where L is the horizontal length scale of the shear which we take as being the radius at the base of the convection zone ($r_{\rm BCZ} \sim 0.71\,{\rm R}_\odot$); hence $l_z \sim 0.002\ r_{\rm BCZ}$. Meanwhile, the thickness of the tachocline has been estimated to be $\delta \sim$ 1-5% of $r_{\rm BCZ}$; hence $\delta \sim 0.01$-$0.05\ r_{\rm BCZ}$. Based on this, we find that the vertical eddy scale is smaller, even if not significantly, than the thickness of the tachocline.

As a conclusion, in the solar tachocline, vertical shear has very little effect on turbulence hence one can focus on horizontal shear instabilities only, and use the associated scaling laws derived by Garaud (2020). But it is also known that the tachocline is an extreme case, with a very strong layer. Other stars do not have such a strong shear layer, as far as we know, and we suspect that the effect of this vertical shear will be even weaker for those. In general terms, our findings show that vertical shear is not very important and that it is sufficient to consider scalings obtained in the pure horizontal shear case, at least when rotation is not important.

Bibliography

Christensen-Dalsgaard, J., Gough, D. O., & Knudstrup, E. 2018, MNRAS, 477, 3845

Cope, L., Garaud, P., & Caulfield, C. P. 2020, Journal of Fluid Mechanics, 903, A1

Elliott, J. R. 1997, A&A, 327, 1222

Garaud, P. 2020, ApJ, 901, 146

Garaud, P., Gagnier, D., & Verhoeven, J. 2017, ApJ, 837, 133

Prat, V. & Lignières, F. 2013, A&A, 551, L3

Prat, V. & Lignières, F. 2014, A&A, 566, A110

Schou, J., Antia, H. M., Basu, S., et al. 1998, ApJ, 505, 390

Spiegel, E. A. & Zahn, J. P. 1992, A&A, 265, 106

Zahn, J. P. 1992, A&A, 265, 115